# Microstructure dependence of magnetization mechanisms in Co-Fe thick films

María del Carmen Aguirre,[1,2,*] Silvia E. Urreta,[2] Paula G. Bercoff[1,2]

[1]Instituto de Física Enrique Gaviola (IFEG), Conicet. Ciudad Universitaria, 5000 Córdoba, Argentina.
[2]Facultad de Matemática, Astronomía, Física y Computación (FAMAF). Universidad Nacional de Córdoba. Ciudad Universitaria, 5000 Córdoba, Argentina.

*Corresponding autor:* María del Carmen Aguirre.
E-mail: carmenaguirre@famaf.unc.edu.ar

## Abstract

Magnetization reversal mechanisms in electrodeposited $Co_{100-x}Fe_x$ (x = 0; 20; 30; 50) films are investigated by measuring the angular dependence of coercivity and relative remanence at room temperature. Deposition is performed onto Cu substrates using the pulse-reverse plating technique under nearly zero-field ($B_0$ condition) and under a constant magnetic field of 100 mT ($B_{100}$ condition), which is applied perpendicular to the Cu substrate, providing different microstructural scenarios according to composition, grain shape and size, film thickness and crystallographic texture. Iron-containing films deposited under the magnetic field are thinner, low textured and exhibit a smaller grain size scale. Films are soft ferromagnetic, with a nearly in-plane easy axis. The $B_{100}$ condition and the iron content promote larger coercivities, independently of composition, the film thickness and the relative orientation between the film plane and the applied field. The angular dependence of coercivity reaches a maximum near 75° - 80° and a minimum near 90°, the hard axis direction. This maximum arises from a transition from a magnetization switching mechanism controlled by domain wall depinning to another one, controlled by inverse domain nucleation inside the grains. This transition is mainly controlled by grain size; it disappears when localized nucleation of inverse domains becomes less competitive (more difficult) by extensive exchange coupling of small grains.

*Keywords*: Electrodeposition; Co-Fe thick films; Field-assisted synthesis; Magnetic hysteresis; Magnetization mechanisms.

## 1-Introduction

Co-Fe alloys are quite important soft magnetic materials because of their unique magnetic properties like large permeability and very high saturation magnetization. Systems based on Co-Fe with different dimensionality like nanoparticles [1], nanowires [2,3] and thin films [4] have been investigated, in particular the influence of microstructure on their hysteresis properties.

On the contrary to ultrathin and thin magnetic films, the magnetization reversal mechanisms leading to the observed hysteresis properties of Co-Fe thick (a few microns) films have not been completely described in relation to microstructural features. It is widely accepted that in thin films the magnetic polarization changes by the mechanism of inverse domain nucleation and domain wall depinning when the applied field is near the hard axis and easy axis, respectively. Based on ferromagnetic resonance and electron spin resonance techniques applied to Co-Fe films from 82 nm to 1756 nm

thick, Cao *et al.* [5] found that the increase of film thickness leads to a larger in-plane anisotropy field, and to a monotonic decrease in coercivity, in both easy and hard axis orientations. Dong *et al.* [6] investigated the polarization reversion mechanism in $Fe_{1.2}Co$ films (~100 nm), finding that the formation and growth of the reversed nucleus played a main role in blocking the motion of domain walls. However, no clear effect of the film thickness or the grain size distribution on coercivity has been reported for thick films and little is known about the details of the polarization reversal mechanisms.

In a previous article [7] we reported the effect of a magnetic field applied perpendicularly to the electrode plane during the electrocrystallization of thick (~ μm) Co-Fe films, prepared by pulse-reverse plating onto Cu foils. Film morphologies and microstructures were found to largely depend on the Fe/Co solution composition and on the magnetic field applied during electrocrystallization. The key factors explaining the influence of the magnetic field and composition on the film deposition mechanisms and microstructure were found to be: local convection nearby the interface, the $H_2$ desorption rate and the competence/interplay of Co(II) and Fe(II) ions during the alloy nucleation and growth.

The particular morphologies and microstructures obtained with this processing route, with different thickness, grain size, composition and crystallographic texture, are interesting structural scenarios in which the competition between the domain wall and granular nucleation mechanisms may be investigated, by measuring the angular dependence of the hysteresis parameters as the coercive field $\mu_0 H_C$ and $S$ ($=M_R/M_S$, with $M_R$ and $M_S$ the remanent and the saturation magnetization, respectively).

In this context, the aim of this work is to explore the magnetization reversal mechanisms responsible for the coercivity and the relative remanence observed in thick Co-Fe films, and to determine their relationship with the film morphology, microstructure and composition.

## 2-Experimental Procedures

$Co_{100-x}Fe_x$ (x = 0; 20; 30; 50) films were prepared by electrodeposition from a $CoCl_2$ 0.1M solution and different 0.1 M $FeSO_4$ solutions, with varied mole ratios (Co/Fe: 100/0, 80/20, 70/30 and 50/50), following the procedure previously reported [7]. A Potentiostat/Galvanostat Autolab 302N was used for the electrodepositions with a reference electrode of Ag/AgCl (3M KCl), an Au spiral as the counter electrode and an electropolished 0.3 mm thick Cu foil (Alfa Aesar, 99.99 %) as the working electrode. The pulse-reverse plating method was applied, using an initial step of -1.3 V/ 7s, and then 100 cycles given by -0.3 V/1.2 s to -1.3 V/12 s, all at room temperature, under inert ($N_2$) atmosphere. A PASCO scientific model EM-8641device, which allows building up a variable gap magnet using two 3/4-inch diameter neodymium-iron magnets on an iron base was used to apply a magnetic field to the electrolytic cell during the syntheses. The electrodepositions were performed without any applied field ($B_0$ condition), and under a constant, uniform field of 100 mT ($B_{100}$ condition). Samples are named after their Co content (x) and the field deposition condition as Co(100-x)-$B_0$ and Co(100-x)-$B_{100}$. Current–time transients (CTT's) measured during the electrodeposition of $Co_{100-x}Fe_x$ films are shown in Fig. S1 of the *Supplementary Information*, for consecutive pulses during a lapse of 60 s. Fig. S1(a) to Fig. S1(d) correspond to samples Co, Co80, Co70 and Co50, respectively, electrodeposited in conditions $B_0$ and $B_{100}$.

A Sigma Zeiss Field Emission-Scanning Electron Microscope (FE-SEM) was used to determine the samples' morphology, and surface conditions. The nominal chemical composition of the different films was determined with an Oxford Energy Dispersive Spectrometer (EDS) by sampling large areas to improve the mean composition accuracy. The results are shown in Fig. S2 of the *Supplementary Information* section, and the composition of Co-Fe films are included in Table 1.

Crystalline structures were determined by X-ray diffraction (XRD) in a Philips PW 1800/10 diffractometer with Cu $K_\alpha$ radiation ($\lambda$ = 1.540 Å).

Magnetic hysteresis loops were measured at room temperature, in a vibrating sample magnetometer VSM Lakeshore 7300, with a maximum field of 1.5 T. Major hysteresis loops were also measured for different values of the angle $\theta$ between the applied magnetic field $B$ and the films planes, varying from 0° to 100°, in 5° steps. Coercivity and relative magnetization were then determined for each orientation.

## 3-Results and Discussion

### *3.1. Microstructure and morphology*

The crystallinity and phases in the different films were investigated by X-ray diffraction in a Bragg-Brentano set up, varying the angular range between $2\theta$=30° and 120°. The indexed patterns obtained for the films prepared in conditions $B_0$ and $B_{100}$ are shown in Fig. 1(a) and Fig. 1(b), respectively.

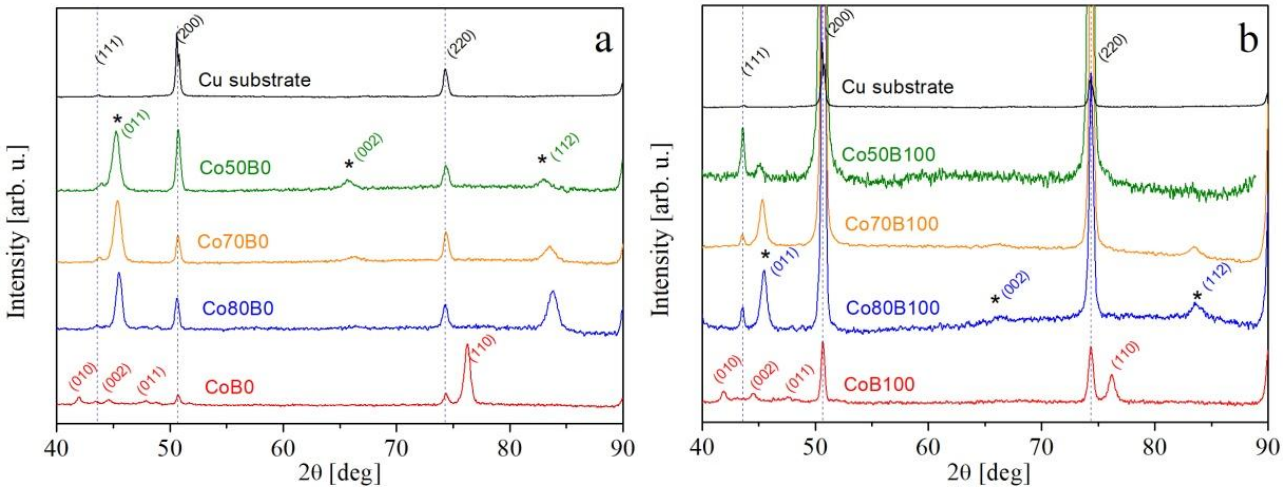


Figure 1. X-ray diffractograms corresponding to Co-Fe films electrodeposited under (a) null applied magnetic field ($B_0$ condition) and (b) a magnetic field of 100 mT ($B_{100}$ condition), normal to the electrode surface. In iron-containing films only a *bcc* Fe(Co) solid solution is detected for all the compositions studied, whose reflection peaks are marked with an asterisk.

Compact *hcp* (JPDS 00-001-1278) and *fcc* cubic (JCPDS 00-015-0806) phases conform pure Co films. In iron-containing films, a *bcc* Fe(Co) solid solution is identified with the following references: CoFe (JCPDS 00-044-1433); $Co_{70}Fe_{30}$ (JCPDS 00-048-1818) and $Co_{80}Fe_{20}$ (JCPDS 00-048-1817). In Co-Fe films electrodeposited at $B_0$, grain size decreases with iron content from 25 to 15 nm; in those produced in $B_{100}$ condition, the size reduces from 31 nm to 10 nm with iron content. Crystallographic texture in the films also decreases with the iron content and in samples of the same composition but deposited under the magnetic field. Both effects are likely to arise from increasing convection currents (gradients in the paramagnetic ions density) and/ micro magnetic hydrodynamic currents nearby the interface, during the film growth [7].

Crystallographic texture $T$ for all the films was estimated using the expression:

$$T\,(hkl) = \frac{\frac{I_{hkl}}{I_{0hkl}}}{\frac{1}{N}\sum_{hkl}\frac{I_{hkl}}{I_{0hkl}}} \qquad (2)$$

where the subscript zero indicates the intensity of the *hkl* peak in the reference card and $N$ is the number of peaks considered for the analysis.

In Co films the volume fractions $f_V$ of each phase were estimated as:

$$f_V^{Co\ hex} = \frac{I_{Co\ hex}^{100}}{I_{Co\ hex}^{100} + I_{Co\ cub}^{100}} \quad (3.a)$$

$$f_V^{Co\ cub} = \frac{I_{Co\ cub}^{100}}{I_{Co\ hex}^{100} + I_{Co\ cub}^{100}}. \quad (3.b)$$

where the superscript 100 refers to the 100% amplitude peak in the corresponding reference card.

Lattice constant values were calculated for each phase in the films, and the mean crystallite size in the direction perpendicular to the film plane was estimated using the Scherrer formula. Differences in the lattice parameters are associated to composition. These results are listed in Table 1 together with the film thicknesses, estimated from SEM images (lateral views).

Table 1. Microstructural parameters of the prepared films. Lattice constants *a* and *c* of the phases in the films, their volume fraction $f_V$, texture index *T* and the corresponding crystallographic direction are listed. Mean film thickness *t*, the crystallite size $d_G$ and the estimated domain wall thickness $\delta_w$ are also listed. N/D stands for 'not detected'.

| *Sample* | Co/Fe | *Phase* | *a* [±0.001 Å] | *T* | *t* [±0.2μm] | $d_G$ [±5nm] | $\delta_w$[±5nm] |
|---|---|---|---|---|---|---|---|
| Co-$B_0$ | 100/0 | *hex* Co | *a* = 2.482 | 3.6 (110) | 1.5 | 24 | 16 |
| | | $f_V$= 84% | *c* = 4.164 | | | | |
| | | *fcc Co* | *a* = 3.599 | 2.7 (220) | | 55 | 23 |
| | | $f_V$ = 16 % | | | | | |
| Co-$B_{100}$ | 100/0 | *hex* Co | *a*=2.488 | 3.6 (110) | 2.3 | 20 | 16 |
| | | $f_V$ = 70% | *c*=4.143 | | | | |
| | | *fcc Co* | *a*=3.608 | 1.8 (220) | | 40 | 23 |
| | | $f_V$ =30 % | | | | | |
| Co80-$B_0$ | 76/24 | *bcc* Fe(Co) | *a*=2.857 | 2.2 (112) | 3.3 | 23 | 51 |
| Co80-$B_{100}$ | 82/18 | *bcc* Fe(Co) | *a*=2.790 | N/D | 0.3 | 18 | |
| Co70-$B_0$ | 69/31 | *bcc* Fe(Co) | *a*=2.826 | 1.2 (112) | 1.4 | 15 | 57 |
| Co70-$B_{100}$ | 68/32 | *bcc* Fe(Co) | *a*=2.829 | N/D | 0.5 | 18 | |
| Co50-$B_0$ | 58/42 | *bcc* Fe(Co) | *a*=2.845 | 1.3 (200) | 1.7 | 15 | 93 |
| Co50-$B_{100}$ | 58/42 | *bcc* Fe(Co) | *a*=2.845 | N/D | 0.9 | 10 | |

Analysis of the patterns in Fig.1 indicates that iron-containing films are single phase, consisting of a *bcc* Fe(Co) solid solution. It is also found that as the iron content increases, the crystalline texture in the films decreases and it almost vanishes in samples electrodeposited under a magnetic field. When deposited under $B_{100}$ condition, the films are thinner. These features are consistent with a delayed nucleation process and a slower growth kinetics in presence of Fe ions, as found in [7]. The *fcc* phase observed in the corresponding patterns of Fig.1 corresponds to the Cu laminated substrate.

Regarding the films morphology, Co-$B_0$ films shown in Fig. 2(a) are relatively dense (see also a lateral view in Fig.2(b)) with structures of 100-400 nm in diameter, as observed in the upper view of Fig. 2(a). Co-$B_{100}$ films electrodeposited under a field of 100 mT also display this dense morphology but surface details are in this case somewhat larger, as observed in Fig.2(c) and Fig.2(d). This

increase in thickness and in the surface feature' size with an applied field is only observed in pure Co films, while the opposite trend is found for the alloyed films.

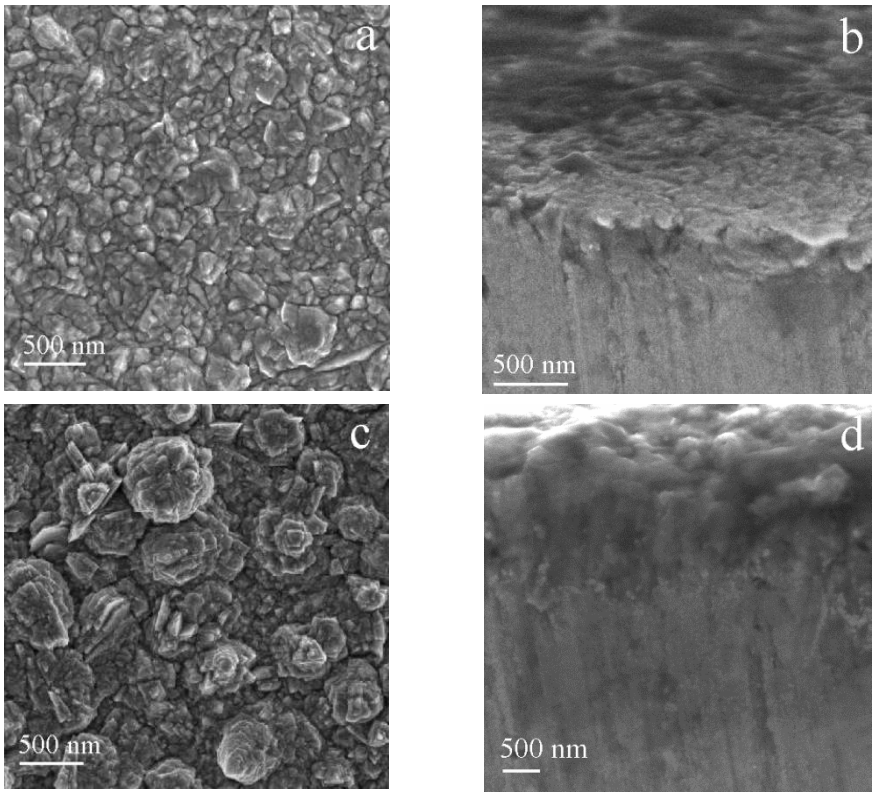


Figure 2. SEM images of Co films prepared by pulse-reverse electrodeposition, onto copper foil substrates, under conditions $B_0$ (a, b) and $B_{100}$ (c, d). Images (b) and (d) are lateral views of the films displayed in (a) and (c), respectively.

It has been demonstrated [7] that the effective ion diffusion coefficient increases with the iron content in the film and becomes larger in $Co_{100-x}$ $Fe_x$ films prepared under a magnetic field ($B_{100}$). Sample Co80-$B_0$ exhibits a less uniform surface –Fig. 3(a)– with highly agglomerated spheroidal grains; it may be also observed that no columnar structure develops but new grains form on top of the old ones Fig 3(b). In condition $B_{100}$, Co80 films are thinner and a smaller mean particle size may be observed in Fig. 3(c) and Fig. 3(d).

The films with larger iron content exhibit an irregular morphology. Fig.4(a) and Fig. 4(b) show, respectively, top and lateral views of a Co70-$B_0$ film. After an initial dense columnar-like microstructure, accounting for a large fraction of the total film thickness, small equiaxed grains develop and in the final stage a dense distribution of interconnected nanowalls of about 200 nm in length and 30 nm thick are observed, which are likely nucleated onto the columnar structure (about 40 nm in diameter).

On the other hand, Co70-$B_{100}$ films exhibit a quite different morphology; top views after 60 s electrodeposition show grain agglomerates, many of them interconnected by very thin whiskers. The lateral view shows such grain agglomerates of about 70 nm in size. These films are thinner than those processed in condition $B_{0,}$ in agreement with a reduced nucleation rate during electrodeposition. Fig.4(c) and Fig. 4(d) display top and lateral views of Co70-$B_{100}$ films, respectively.

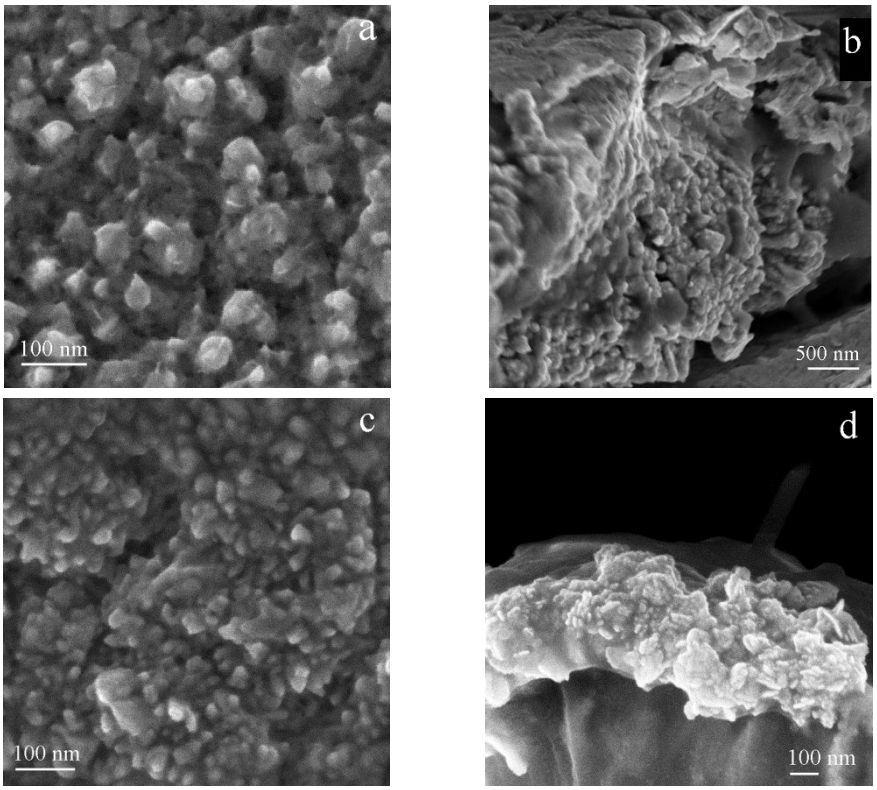


Figure 3. Co80 films obtained in conditions $B_0$ (a, b) and $B_{100}$ (c, d). Images (b) and (d) correspond to lateral views.

The film with equiatomic composition Co50-$B_0$ –Fig.5(a) and Fig.5(b)– exhibits similar features than Co70-$B_0$. In this sample, uniformly distributed inter-connected nanowalls (120 nm in length, 20-25 nm in thickness) cover the surface, giving the film a complex texture. On the contrary, film Co50-$B_{100}$ –Fig.5(c) and Fig.5(d)– display a more regular, granular structure (particles ~20-30 nm in size).

In samples prepared under $B_0$ condition, the morphology changes from quite columnar grains, normal to the film plane (Co), to a granular superficial layer (Fe ≥ 30%). On the contrary, the films are essentially granular for the $B_{100}$ condition for all compositions, exhibiting smaller grain size as the Fe content in the alloy increases.

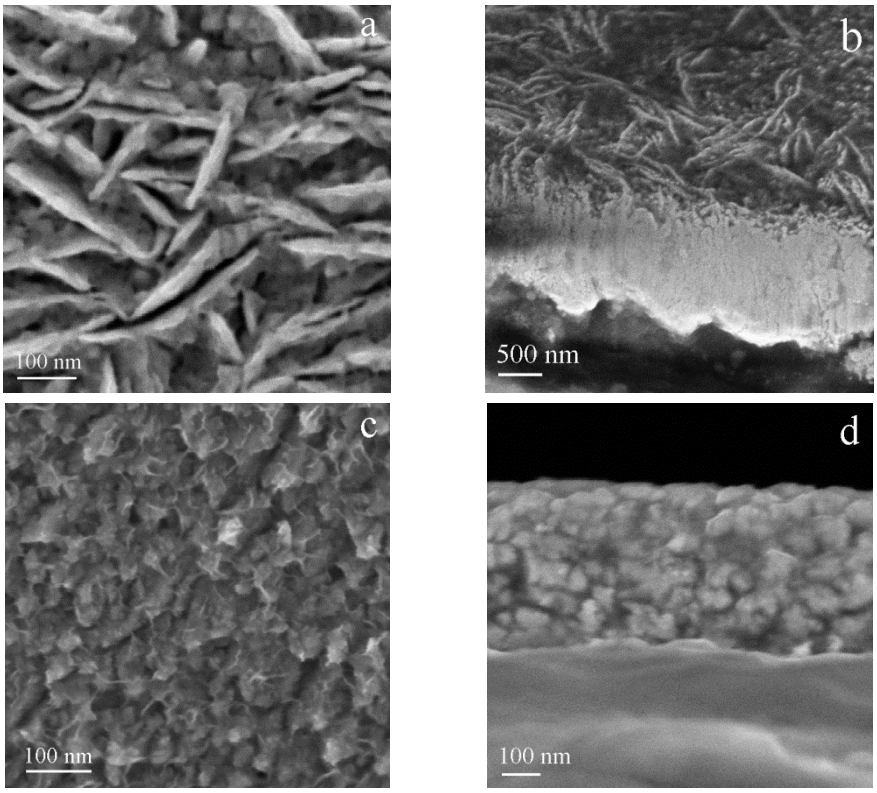


Figure 4. Top view of films (a) Co70-$B_0$ and (c) Co70-$B_{100}$. Images (b) and (d) correspond to lateral views of the films shown in (a) and (c), respectively.

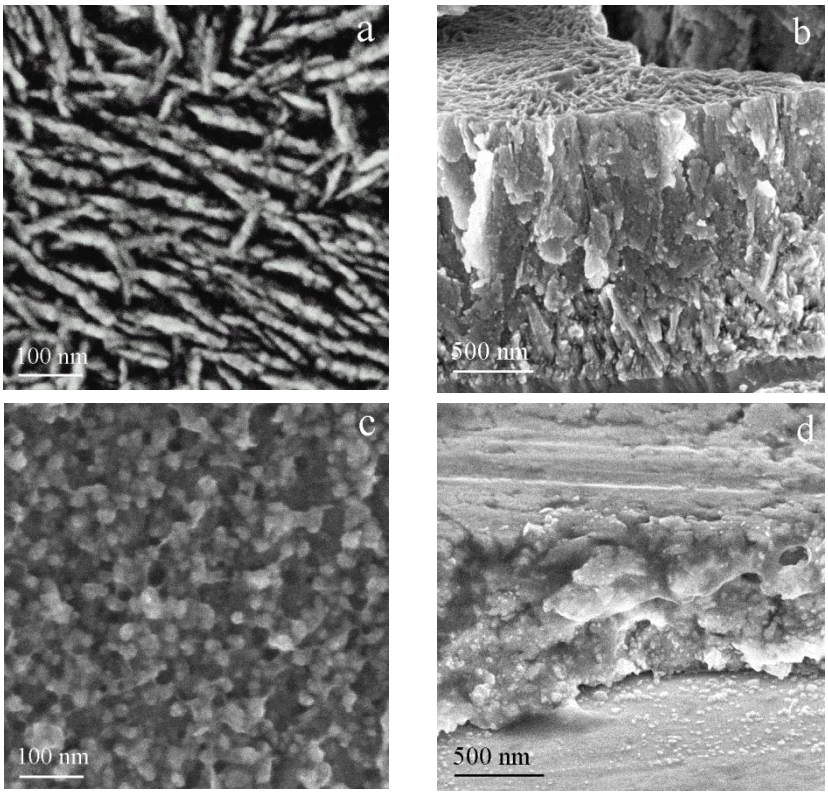


Figure 5. Top view of films (a) Co50-$B_0$ and (c) Co50-$B_{100}$. Lateral views of the films shown in (a) and (c) are depicted in images (b) and (d), respectively.

*3.2. Magnetic properties*

A magnetic field of 100 mT applied during electrodeposition changes the kinetics of the alloy crystallization reactions and consequently the deposit microstructure and morphology, so different magnetization reversal behaviors may be expected.

Magnetic hysteresis properties were characterized by the coercivity $\mu_0 H_C$ (the applied field at which magnetization $M = 0$) and the relative remanent magnetic moment $S = M_R/M_S$ ($S$ is the loop squareness, $M_R$ and $M_S$ are the remanent and saturation magnetization, respectively), taken from the room temperature $M$-$H$ major loops. Magnetization mechanisms were explored by measuring the coercive field and the relative remanence both as functions of the angle between the film plane and the applied magnetic field. Fig. 6(a) to Fig. 6(d) show the hysteresis loops for two relative field orientations, parallel (PA, $\theta = 0$) and perpendicular (PE, $\theta = 90°$) to the film plane. No corrections to the applied field by the demagnetizing factor and its angular variation [8] were performed to estimate the actual (true) internal field so, shape demagnetizing effects affecting the apparent hysteresis parameters' values cannot be excluded.

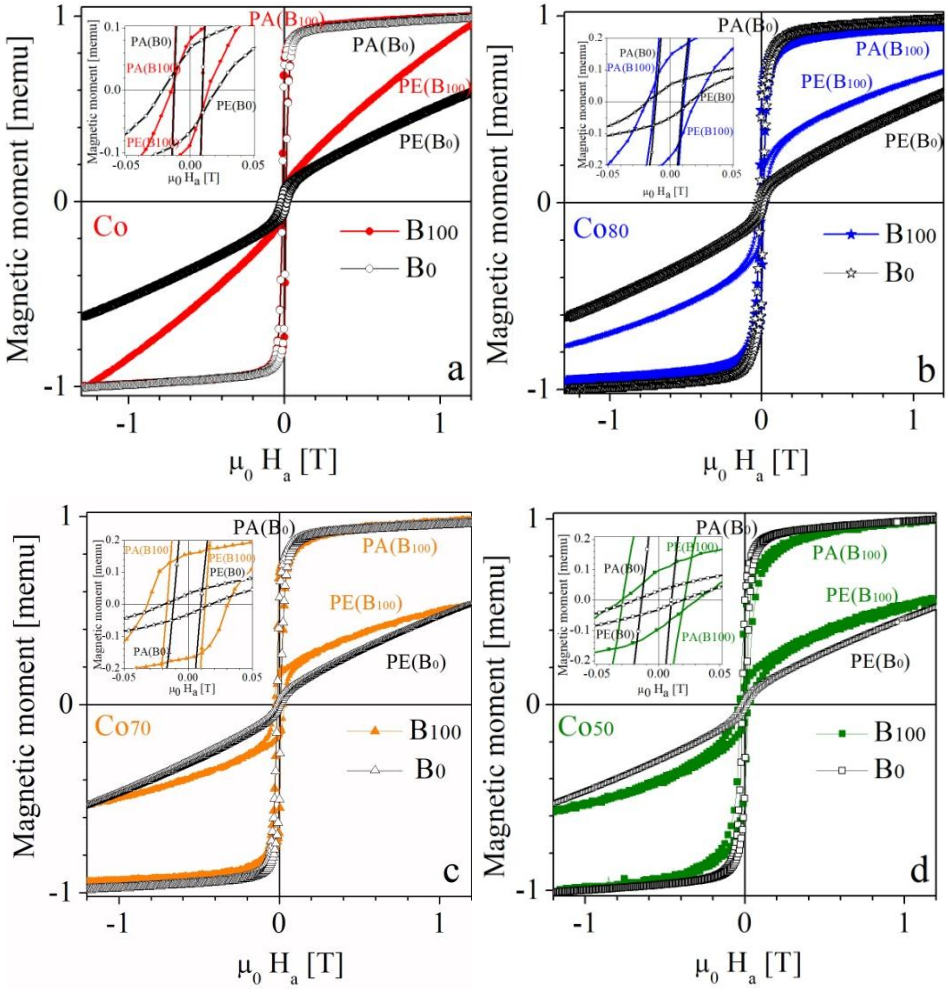


Figure 6. Hysteresis loops corresponding to films (a) Co, (b) Co80 (c) Co70 and (d) Co50 synthesized under $B_0$ and $B_{100}$ conditions, measured with the field applied in directions parallel (PA) and perpendicular (PE) to the film plane. The corresponding insets display a close-up of the low-field region, where the coercivity and relative remanence can be noticed.

Films of different compositions, electrodeposited in $B_0$ and $B_{100}$ conditions, are all magnetically soft, and exhibit easy axis behavior at/near an in-plane direction (PA, $\theta = 0$). The corresponding hysteresis parameters are given in Table 2.

Table 2. Magnetic hysteresis parameters: coercive fields $\mu_0 H_C(\theta = 0)$ and $\mu_0 H_C(\theta = \theta_{max})$; the angle at which the coercive field is maximum ($\theta_{max}$) and minimum ($\theta_{min}$); the relative remanence values at $\theta = 0$, $S(0)$; and at the angles corresponding to the maximum $\theta(S_{max})$ and minimum $\theta(S_{min})$ $S$ values.

| Sample | *Coercivity* | | | | *Relative remanence* | | |
|---|---|---|---|---|---|---|---|
| | $\mu_0 H_C(0)$ [mT] | $\theta_{max}$ [deg] | $\theta_{min}$ [deg] | $\mu_0 H_C(\theta_{max})$ [mT] | $S(0)$ | $\theta(S_{max})$ [deg] | $\theta(S_{min})$ [deg] |
| Co-$B_0$ | 3.9 | - | - | - | 0.1 | 8 | 90 |
| Co-$B_{100}$ | 9.1 | 80 | 90 | 28 | 0.7 | ~0 | 90 |
| Co80-$B_0$ | 2.7 | 74 | 81 | 10 | 0.4 | ~0 | 86 |
| Co80-$B_{100}$ | 4.2 | 75 | 85 | 13 | 0.4 | ~0 | 85 |
| Co70-$B_0$ | 2.7 | 75 | 85 | 8 | 0.2 | ~0 | 85 |
| Co70-$B_{100}$ | 5.2 | 75 | 85 | 25 | 0.6 | ~0 | 85 |
| Co50-$B_0$ | 3.6 | - | - | - | 0.3 | ~0 | 85 |
| Co50-$B_{100}$ | 10.2 | 80 | 85 | 29 | 0.4 | ~0 | 85 |

The deposited films are relatively thick (in the order of a few μm), so no large effects of their thickness through surface anisotropy on the coercive field may be expected [9]. Assuming also negligible magneto-elastic contributions, the effective magnetic anisotropy $K_{eff}$ is likely to arise from the interplay between magnetocrystalline and magnetostatic (mainly shape anisotropy) contributions, being the former more important in Co films and the latter in Fe-containing ones.

The dependence of both, coercivity and squareness $S$, on the angle $\theta$ between the external applied field and the film plane were measured at room temperature and the results are shown in Fig. 7. This angular dependence provides information about the actual orientation of the effective easy axis in the samples (aligned near the angle at which $S$ has a local maximum) and also allows exploring the magnetic polarization reversal mechanisms controlling coercivity.

Fig. 7(a) displays the coercive field as a function of the angle $\theta$, showing in some cases a non-monotonic behavior, often observed in thin films [9-11]. The peak observed in $\mu_0 H_C$ vs. $\theta$ in the range $0 < \theta < 90°$ is generally explained on the basis of a transition in the controlling reversal mechanism responsible for coercivity. The different behaviors observed in Fig. 7(a) may be then explained by the film morphology and/or microstructure, as these factors determine which magnetization reversal mechanism becomes competitive for each angular configuration of the applied field.

As mentioned before, the films studied in this work are not thin, but exhibit thicknesses between 0.4 μm and 2 μm, largely exceeding the domain wall size $\delta_W$ ($= \pi\sqrt{A/K}$, with $A$ and $K$ the exchange and the magnetocrystalline energy constants, respectively [9 Ohandley]) along the three directions. Regarding the microstructure, the films are polycrystalline with grain/crystallite sizes between 55 nm and 10 nm, depending on the iron content. Then, grains are larger than $2l_{ex}$ ($l_{ex} = \sqrt{\frac{2A}{\mu_0 M_S^2}}$ is the magnetic exchange length in the material) in Co films ($l_{ex}$ = 3.4 nm) and Co80 films ($l_{ex}$ = 3.23 nm),

while in Fe richer films such as Co70 ($l_{ex}$ = 2.92 nm) and in Co50 ($l_{ex}$= 2.56 nm) the smaller grain size becomes comparable to $2l_{ex}$, suggesting that intergranular exchange coupling becomes more important. Bloch domain-wall thicknesses, estimated from parameters taken from ref. [9], are comparable to or even larger than the crystallite sizes, except perhaps in pure Co films (see Table 1).

Two types of $\mu_0 H_C$ vs. $\theta$ curves are observed in the present work: one with coercivity monotonously increasing with the angle, leading to a so-called '*bell-type*' profile between 0° and 180° and another one, going through a sharp maximum at $\theta_{max}$ and a local minimum near the theoretical magnetostatic hard direction at $\theta_{min}$ in the film, exhibiting an *'M-type'* dependence in the same angular range.

L. Xi *et al.* [14,15] also propose that the local maximum in the angular dependence of coercivity, 75°-85° in our case, arises from two different magnetization reversal mechanisms taking place sequentially. When the applied field is close to the easy axis (near an in-plane direction), magnetization is likely to reverse by domain-wall depinning/displacement. On the other hand, when the applied field direction approaches the hard axis (out-of-plane direction), the in-plane field component becomes not strong enough to free and move domain walls, and the dominant magnetization reversal mechanism changes to the nucleation of inverse domains by localized, mainly curling rotation, and the further expansion of domain-wall-like configurations inside the grains. The angle near which the transition between these two mechanisms takes place is $\theta_{max}$, where the coercivity reaches a maximum. Both $\theta_{max}$ and the angle at which coercivity reaches a local minimum around 90°, $\theta_{min}$, corresponding to the apparent hard axis direction, are listed in Table 2.

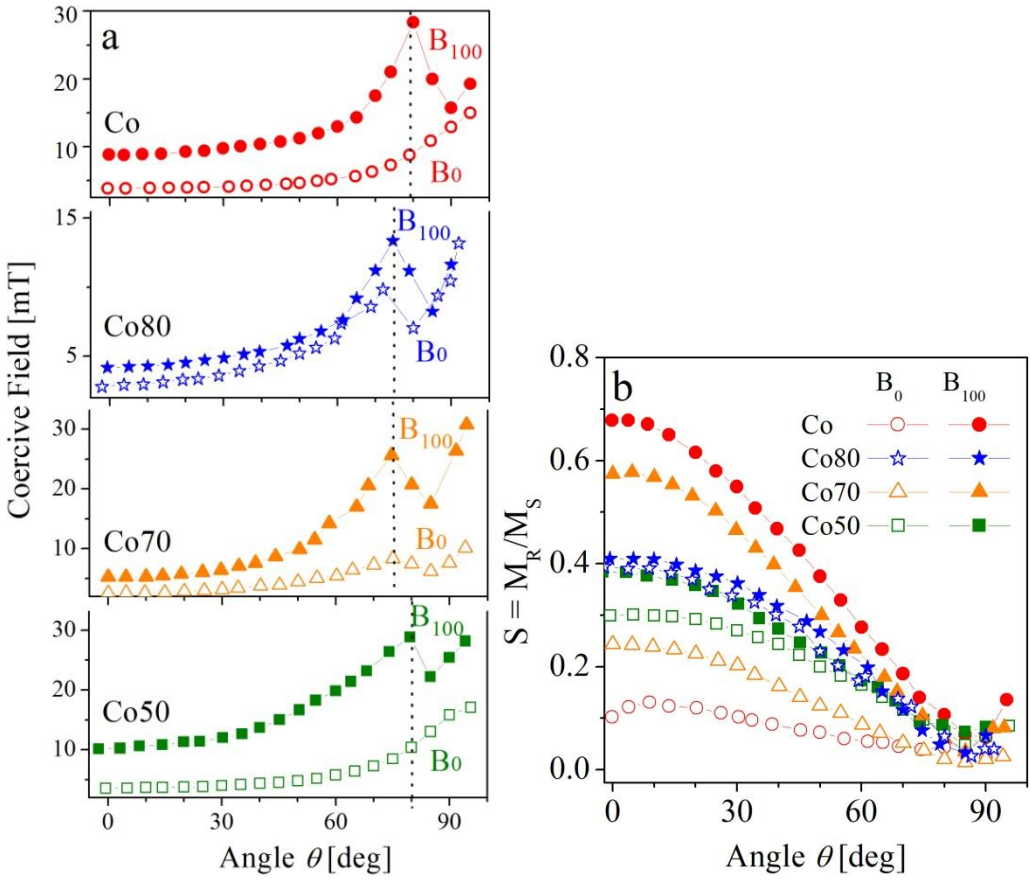


Figure 7. Coercivity (a) and relative remanence (b) as functions of the angle between the applied magnetic field and the sample plane.

A first insight into the role of the film microstructure in determining the characteristics of $\mu_0 H_C(\theta)$ curves was provided by simulations reported by J-G. Zhu [12] for longitudinal thin film media, many years ago. The proposed model predicts that, for a *thin* film with 3D randomly oriented grains, the coercive field as a function of the angle between the applied field and the film plane exhibits an '*M-type'* curve. Two parameters are considered in this analysis, the first of which is $h_m = M_S^2/2K = M_S/H_K$ (where $H_K = 2K/M_S$ is the crystalline anisotropy field); $h_m$ gives a relative measure of the magnetostatic interaction strength to the local crystalline anisotropy in the film. The other parameter is a relative measure of the intergranular exchange interaction strength to the local magnetocrystalline anisotropy constraint, and it is defined as $h_e = A^*/K\alpha^2$, where A* is an effective intergranular exchange energy constant and $\alpha$ is the mean distance between nearest neighbor grains, related to the mean grain size ($\alpha \sim d_G$). As $h_m = M_S/H_K$ increases, when magnetostatic effects become more important as compared to the magnetocrystalline anisotropy field, the angle for the coercivity maximum $\theta_{max}$ gradually shifts towards 90°. Increasing values of $h_e = A^*/Kd_G^2$ (i.e., larger intergranular exchange coupling and lower crystalline anisotropy) makes granular rotation a less competitive mechanism in the film, leaving domain wall depinning as the coercivity controlling mechanism.

Our results for all the films prepared under condition $B_{100}$ are consistent with a change in the coercivity mechanism as the field direction rotates from parallel to perpendicular to the film plane. This means that films with high, domain-wall-controlled coercivity, are likely to experience a change to another mechanism with lower critical field as the in-plane field component decreases. On the contrary, when wall pinning is less effective or nucleation by localized rotation modes is relatively hardened (for example by exchange-coupled grains) no mechanism transition takes place and coercivity monotonously increases with the angle from the easy to the hard direction.

In the present case, when the film thickness reduces, a noticeable increase in coercivity is observed. In fact, coercive fields corresponding to $B_{100}$ samples are always larger, and follow an '*M-type'* curve as function of the angle between the applied field and the film plane, independently of composition, orientation angle and/or thickness. This is consistent with the smaller microstructural size scale observed in $B_{100}$ samples. In fact, grain boundaries act as efficient pinning sites for domain walls, hindering their displacement and increasing coercivity. When grain size is larger than the domain wall, the relationship between the coercivity and the reciprocal of the grain size is given by [13,14]:

$$H_C \approx 3\,\frac{\gamma_w}{M_S}\frac{1}{d_G} \approx 3\sqrt{\frac{k\,T_C\,K}{a\,M_S}}\frac{1}{d_G} \qquad (4)$$

where $\gamma_w$ is the domain wall energy density, $T_C$ the Curie temperature and $a$ is the corresponding lattice constant. On the contrary, when domain walls contain many grains inside them, a lower wall mobility is expected when grain size reduces because a larger fraction of the wall thickness is occupied by pinning defects, also leading to an increasing coercive field. Coercivity also increases with the iron content in the films, mainly due to the growing contribution of shape anisotropy, depending on saturation magnetization. The low crystalline anisotropy becomes even weaker with the reduction in grain size, because of random anisotropy effects.

Unlike sample Co-$B_{100}$, which exhibits a transition between different reversal mechanisms, sample Co-$B_0$ exhibits no transition, being domain wall displacement the dominant mechanism in the complete range, in agreement with more uniform and larger crystallite sizes.

In samples containing 20 at. % Fe (Co80), $B_0$ and $B_{100}$ films exhibit quite similar behaviors, that is, '*M-type'* profiles between 0 - 180°, with well-defined values of $\theta_{max}$ and $\theta_{min}$. In both films, the grain size is somewhat smaller than the domain wall thickness, which is larger because of the lower magnetocrystalline anisotropy, but it is similar in the two field conditions and coercivity values are also comparable.

As the iron content in $B_0$ films increases, the coercive field as a function of $\theta$ gradually changes from '*M-type*' in Co80-$B_0$ to *'bell-type'* in Co50-$B_0$, indicating that in these latter films, domain wall displacement controls coercivity in the whole angular range, and no mechanism transition takes place. In fact, the curves for Co70-$B_0$ and Co50-$B_0$ films tend to become monotonic, with coercivities increasing up to the theoretical hard axis angle (~90°), that is, a *'bell-type'* profile in the 0 - 180° angular range. In these films, the magnetocrystalline anisotropy reduces to values lower than that of iron (-0.4 to -0.15 $10^5$ J/m$^3$[9]) because of random anisotropy as grain size becomes comparable to 2 $l_{ex}$, indicating that even when domain walls may be more strongly pinned by grain boundaries, local nucleation of inverse domains becomes more difficult because of highly exchange-coupled grains and this phenomenon is known to favor a wall-displacement mechanism [12].

The corresponding reduced remanence as a function of $\theta$ is displayed in Fig. 7(b). All the films (except Co-$B_0$) exhibit the maximum in S nearby $\theta \cong 0$ and then the curve follows a similar dependence as expected for the case of an in-plane uniaxial anisotropy. On the other hand, in sample Co-$B_0$ which has a predominant *hcp* Co phase which is largely textured, the maximum in $S(\theta)$ shifts a few degrees (~8°) out of plane. Nevertheless, no clear correlation between the film texture and the easy axis orientation away from the film plane could be established.

## Conclusion

Co and Co-Fe films hysteresis loops, measured at different orientations of the film plane relative to the applied magnetic field indicate that films have a near in-plane ($\theta$= 0°) effective easy axis. Coercivity increases with iron content in the alloy and it is larger in samples deposited under magnetic field, which are thinner in every case. This behavior is rationalized by considering the enhanced domain wall pinning in small-grained films and the contribution to the effective anisotropy of magnetostatic effects, through the increment in the saturation magnetization with increasing iron composition. At low angles, the coercive field is controlled by domain wall depinning in all the films. As the angle increases towards that corresponding to the theoretical hard direction ($\theta$ = 90°), two possible behaviors may take place. The coercive field may increase continuously as expected for a domain wall depinning mechanism or it may undergo a transition from the initial magnetization switching mechanism to another one, likely involving inverse domains nucleation by localized non-uniform rotation (mainly curling) inside the grains. All the iron-containing films prepared under the external magnetic field, with smaller, randomly oriented grains perform this mechanism transition. The key parameters selecting the magnetization reversal mechanisms that control coercivity are found to be composition and the mean grain size.

## Declaration of Competing Interest

The authors declare that they have no known competing financial interests or personal relationships that could have appeared to influence the work reported in this paper.


## Acknowledgements

This work has been partially supported by Secyt - Universidad Nacional de Córdoba, ANPCyT-FONCyT through project PICT 2015-0135 and Conicet, Argentina.


## References


[1] Jinu Kim, Jinbae Kim, Jongryoul Kim, Ki Hyeon Kim. Characterization of as synthesized FeCo magnetic nanoparticles by coprecipitation, J. Appl. Phys. (2013)113, 17 A313. DOI: 10.1063/1.4795321.

[2] D. H. Qin, L. Cao, Q. Y. Sun, Y. Huang, H. L. Li, Fine magnetic properties obtained in FeCo alloy nanowire arrays, Chem. Phys. Lett. 358 (2002) 484–488. DOI:10.1016/S0009-2614(02)00649-8.
[3] M. S. Viqueira, N. Bajales, S. E. Urreta, P. G. Bercoff, Magnetization mechanisms in ordered arrays of polycrystalline $Fe_{100-x}Co_x$ nanowires, J. Appl. Phys.117 (2015) 204302. DOI: 10.1063/1.4921701.
[4] D. Zhou, M. Zhou, M. Zhu, X. Yang, M. Yue, Electrodeposition and magnetic properties of FeCo alloy films, J. Appl. Phys. 111 (2012) 07A319-1-3. DOI: 10.1063/1.3675063.
[5] D. Cao, X. Cheng, H. Feng, C. Jin, Z. Zhu, L. Pan, Z. Wang, J. Wang, Q. Liu, Investigation on the structure and dynamic magnetic properties of FeCo films with different thicknesses by vector network analyzer and electron spin resonance spectroscopy, J. All. Comp. 688 (2016) 917-922. DOI: 10.1016/j.jallcom.2016.07.110.
[6] D. Dong, Q. Fang, W. Wang, J.Yang. Temperature Characteristics and Magnetization Mechanism of $Fe_{1.2}Co$ Films, J. Mag. Magn. Mat. 442 (15) (2017) 295-299. DOI: 10.1016/j.jmmm.2017.04.071.
[7] M. del C. Aguirre, S. E. Urreta, Effect of an external magnetic field orthogonal to the electrode surface on the electro-crystallization mechanism of Co-Fe films under pulsed applied potential. J. All. Comp. 878 (2021) 160347-160360. DOI: 10.1016/j.jallcom.2021.160347.
[8] M. Huang, J. H. Judy, Calculations of the angular dependence of apparent and true coercivities of thin film magnetic recording media, IEEE Trans. Mag. 29(6) (1993) 4083-85. DOI: 10.1109/20.281397
[9] X. Han, J. Ma, Z. Wang, Y.Zuo, L. Xi, In-plane uniaxial anisotropy and magnetization reversal mechanism of FeCo films by strip pattern, Acta Metall. Sin. (Engl. Lett.) 27 (6) (2014) 1099–1104. DOI:10.1007/s40195-014-0131-6.
[10] R. C. O'Handley, Modern magnetic materials: Principles and applications. 2000 (Chap. 16), pp 328, pp375, John Wiley and Sons, New York.
[11] J. S. Gau, C. F. Brucker, Angular variation of the coercivity in magnetic recording thin films, Journal of Applied Physics 57 (1985) 3988-3990. DOI: 10.1063/1.334885.
[12] P. Prieto, J. Camarero, J. F. Marco, E. Jiménez, J. M. Benayas, J. M. Sanz, Characterization of nanocrystalline permalloy thin films obtained by nitrogen IBAD, IEEE Trans. Mag. 44(11) (2008) 3913-3916. DOI:10.1109/TMAG.2008.2002483.
[13] J-G. Zhu, Coercivity angular dependence in longitudinal thin film media, J. Mag. Magn. Mat. 109 (1992) 367-374. DOI: 10.1016/0304-8853(92)91775-O.
[14] L. Xi, J.H. Du, J.J. Zhou, J.H. Ma, X.Y. Li, Z. Wang, Y.L. Zuo, D.S. Xue, Soft magnetic property and magnetization reversal mechanism of Sm doped FeCo thin film for high-frequency application, Thin Solid Films 520 (2012)5421-5425. DOI: 10.1016/j.tsf.2012.04.013.
[15] L. Xi, Q.J. Sun, X.Y. Li, J.J. Zhou, J.H. Du, J.H. Ma, Z. Wang, X.N. Shi, Y.L. Zuo, D.S. Xue, Recovery of soft magnetic properties of FeNiSm films by Ta interlayer, J. Mag. Magn. Mat. 323(16) (2011) 2219-2223. DOI: 10.1016/j.jmmm.2011.03.039.
[16] J-G. Zhu, Coercivity angular dependence in longitudinal thin film media, J. Mag. Magn. Mat. 109 (1992) 367-374. DOI: 10.1016/0304-8853(92)91775-O.
[17] A. Mager, About the influence of the grain size in the coercive force, Ann. der Physik (Leipzig) 446(1) (1952) 15-16. DOI: 10.1002/andp.19524460104.
[18] H. Yu, S. Basu, Y. Zhang, A. Parvizi-Majidi, J. Q. Xiao. Pinning effect of the grain boundaries on magnetic domain wall in FeCo-based magnetic alloys, J. Appl. Phys. 85 (1999) 6655. DOI: 10.1063/1.370175.

†††

# *Supplementary Information*

The analysis of the transients was performed for the cathodic pulse region (between -0.006 A $cm^{-2}$ to -0.008 A $cm^{-2}$, see insets in Figs S.1). As it was previously reported by us in ref. [7], in the analysis of current-time curves it was applied a modification of the nucleation-and-growth generalized model proposed by B. R. Scharifker and J. Mostany, where the contribution of the hydrogen co-reduction to the total current was considered [ref. S1 and S2].

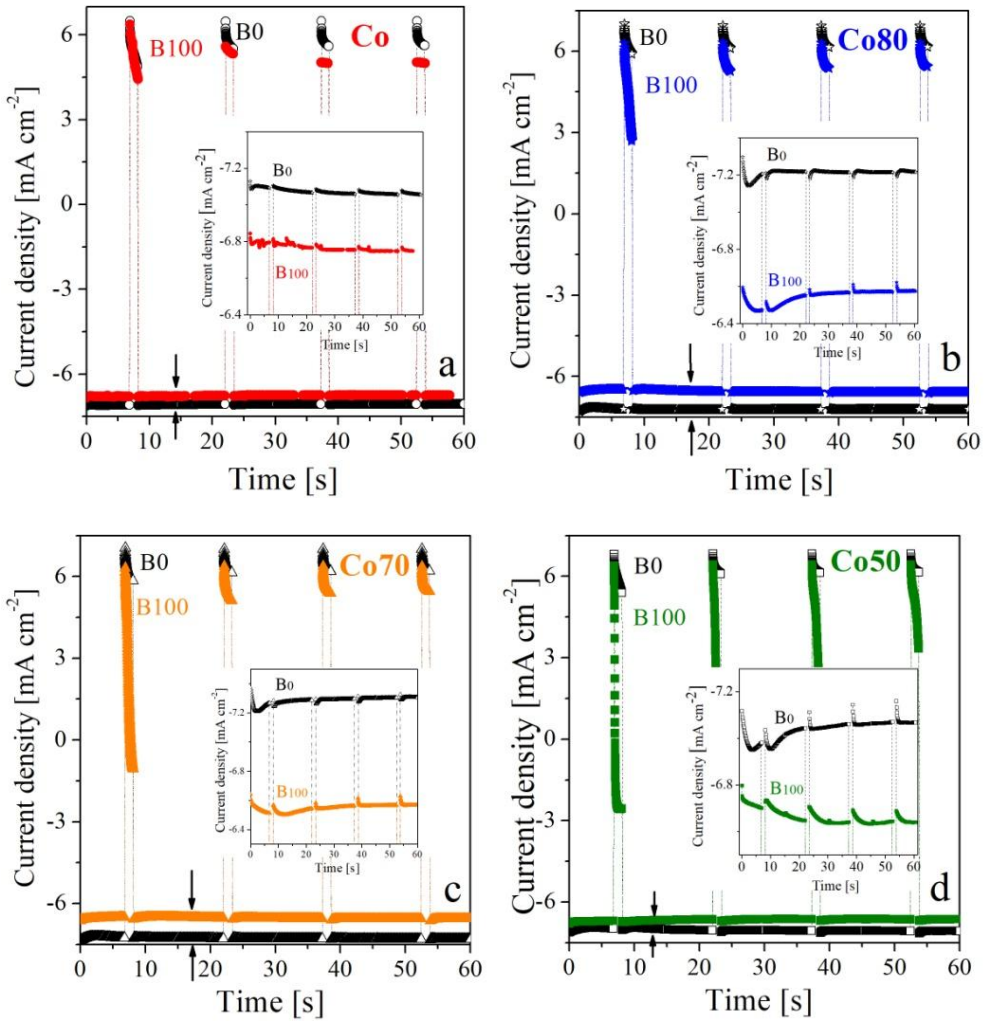


Figure S1. CTT's measured under $B_0$ and $B_{100}$ conditions for 60 s: (a) pure Co and bimetallic films (b) Co80, (c) Co70 and (d) Co50. The vertical arrows shown at the bottom of each graph indicate the scale that has been enlarged in each figure's inset.

As reported in ref. [7], all Co and Co-Fe films electro crystallized through a 3D diffusional growth regime. Among the constants determined by nonlinear fitting of theoretical models to experimental results, the nucleation rate constant or nucleation frequency $A$ ($s^{-1}$) was the key parameter to evaluate the nucleation mechanism. It is found that under a magnetic field of 100 mT, nucleation is instantaneous for a single element like Co, with $A>>1$, but it gradually changes to progressive as the iron content increases, becoming $A << 1$ for Co50. In the absence of a magnetic field ($B_0$), a progressive nucleation predominates for Co ($A << 1$), turning to a more instantaneous behavior in presence of iron, with $A > 1$. The magnetic field and the iron content are then decisive in selecting

both nucleation and film-growth regimes. Iron concentration reduces the number density of active sites for nucleation $N_0$ ($cm^{-2}$) and nucleation rates per site $AN_0$ ($cm^{-2}\ s^{-1}$), being this effect even more noticeable when the perpendicular magnetic flux is acting ($B_{100}$ condition). This reduction in $AN_0$ affects the film morphology as well as the particles size and shape. Co-rich films exhibit a granular morphology, changing to a dendritic-like one in films with an increasing iron concentration. Moreover, size scale in iron-rich samples becomes smaller and the film thickness is reduced under $B_{100}$ condition. For iron-rich samples (i.e., Co70 and Co50) it was proposed that a tip-discharge phenomenon took place during the electrodeposition, leading to dendrites formation and the ions depletion at the electrode surface promoted a diffusion-controlled growth. It was demonstrated, when the tip-discharge is strong as in the condition $B_0$, narrow nanowalls are built. Then, for the condition $B_{100}$ when the tip-discharge is weaker, the dendrites grows to a network whiskers-like. The effects of the magnetic flux normal to the electrode surface are explained by considering a delayed nucleation process, due to a micro-magnetic hydrodynamic effect inside of the diffusion layer and to the released hydrogen of the electrode surface [7].

***

A Sigma Zeiss Field Emission-Scanning Electron Microscope (FE-SEM), with an Oxford Energy Dispersive Spectrometer (EDS) was used to observe the morphology and determine the chemical composition of alloys in the different Co/Fe mol ratios. With the ESD, the elemental composition of each sample in specific areas was analyzed. The results of the measurements are shown in the spectra of Figures 1S, which are labeled with the feeding solution composition: (a) Co-$B_{100}$, (b) Co-$B_0$, (c) Co80-$B_{100}$, (d) Co80-$B_0$, (e) Co70-$B_{100}$, (f) Co70-$B_0$, (g) Co50-$B_{100}$, (h) Co50-$B_0$. In the insets of the Figures 1S, the bar graphic indicates the weight percent of each element in the sample, which is given by the equipment software. The normalization and the conversion of Co and Fe at mole percentage provides the real composition of CoFe alloy in the films. These compositions are detailed in the caption of Figure S1 (a),(b),(c),(d),(e),(f),(g),(h) and summarized in Table S1. It is observed that the composition of thick films is $Co_{100-x}Fe_x$ without oxidation, and it is very close to that of the electrolytic bath. The percentage of oxygen is negligible (< 0.6 %), which assured the alloy composition.

**Table S1**. Composition of CoFe films estimated by EDS measurements

| N° | Fed Composition | Real Composition |
|---|---|---|
| a | Co-$B_{100}$ | Co |
| b | Co-$B_0$ | Co |
| c | Co80-$B_{100}$ | $Co_{80}Fe_{20}$ |
| d | Co80-$B_0$ | $Co_{76}Fe_{24}$ |
| e | Co70-$B_{100}$ | $Co_{69}Fe_{31}$ |
| f | Co70-$B_0$ | $Co_{68}Fe_{32}$ |
| g | Co50-$B_{100}$ | $Co_{52}Fe_{48}$ |
| h | Co50-$B_0$ | $Co_{52}Fe_{48}$ |

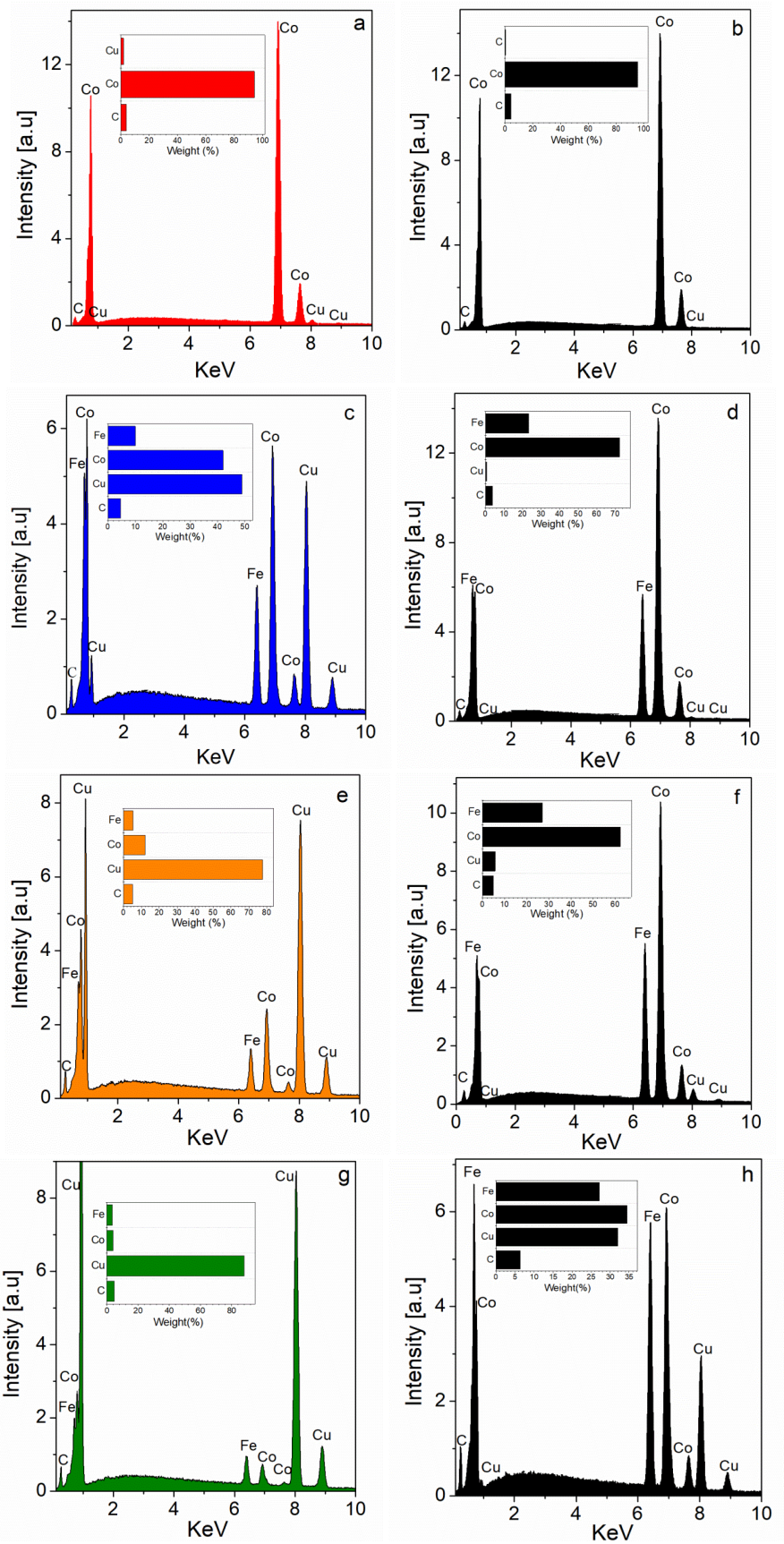


**Figure S2**. a) Co-$B_{100}$ , b)Co-$B_0$ , c) $Co_{80}Fe_{20}$-$B_{100}$, d) $Co_{76}Fe_{24}$-$B_0$, e) $Co_{69}Fe_{31}$-$B_{100}$, f) $Co_{68}Fe_{32}$-$B_0$, g) $Co_{52}Fe_{48}$-$B_{100}$, h)$Co_{52}Fe_{48}$-$B_0$.

## References.

[S1] B. R. Scharifker, J. Mostany, Three-dimensional nucleation with diffusion-controlled growth. Part I. Number density of active sites and nucleation rates per site, J. Electroanal. Chem. 177 (1984) 13-23. DOI: 10.1016/0022-0728(84)80207-7.

[S2] M. Palomar –Pardavé, B.R. Scharifker, E.M. Arce, M. Romero-Romo, Nucleation and diffusion-controlled growth of electroactive centers. Reduction of protons during cobalt electrodeposition, Electrochim. Acta 50 (2005) 4736-474. DOI: 10.1016/j.electacta.2005.03.004